Flux Observer Based on Enhanced Second-Order Generalized Integrator With Limit Cycle Oscillator for Sensorless PMSM Drives

Siqi Wang, Dawei Ding, Guoqiang Zhang, *Senior Member, IEEE*, Binxing Li, Qiwei Wang, Gaolin Wang, *Senior Member, IEEE*, and Dianguo Xu, *Fellow, IEEE*

***Abstract*—In a position sensorless permanent magnet synchronous motor (PMSM) drive system, parameter mismatch will introduce estimation error in the stator flux and rotor position information. A novel flux observer based on an enhanced second-order generalized integrator (SOGI) with a limit cycle oscillator is proposed to improve the robustness of sensorless PMSM drives. Based on the SOGI structure, the proposed method constructs a nonlinear oscillator with a self-excited oscillation function that can maintain the flux trajectory oscillation even in the absence of the input stator electromotive force. The enhanced observer can converge the stator flux trajectory to its expected state under external disturbances and reduce position estimation error. Moreover, the proposed limit cycle oscillator can improve the harmonic suppression ability of the SOGI-based flux observer. The convergence and robustness of the enhanced observer are both investigated, demonstrating that the proposed method can improve the performance of the flux observer. The effectiveness of this method is verified by experiments on a 2.2-kW PMSM drive platform.**

***Index Terms*—Flux observer, nonlinear oscillator, permanent magnet synchronous motor (PMSM), second-order generalized integrator (SOGI), sensorless control.**

I. Introduction

PERMANENT magnet synchronous motor (PMSM) has been widely used in industrial applications and other fields due to the advantages of high efficiency and power density [1], [2], [3], [4]. In order to enhance the robustness, the position sensorless control algorithms have been widely studied. Generally, the rotor position and speed estimation accuracy of sensorless PMSM drives are affected by various nonideal factors (especially the motor parameter mismatch), thereby reducing the control performance of the drive system. Therefore, the research on position sensorless control algorithms with lower estimation error and stronger disturbance suppression ability has been a research hotspot in recent years [5], [6], [7], [8].

There are mainly two types of sensorless algorithms for PMSM drives according to whether additional signals are injected: the high-frequency (HF) injection methods [9] and the model-based methods [10]. In general, HF methods are used for position estimation at zero and low-speed operation regions, but the injected HF signal introduces additional power loss, torque ripple, and HF noise. Model-based methods mainly obtain the rotor position information by observing motor back-EMF or magnetic flux, which are used for medium and high-speed operation regions. The back electromotive force (EMF) model-based methods have the advantages of simple structure and easy implementation, mainly including sliding-mode observers [11], Luenberger observers [12], and extended Kalman filter observers [13]. In the presence of noise introduced by inverter nonlinearity, parameter mismatch, and sampling errors in the drive system, the signal-to-noise ratio of the back-EMF signal decreases. Then the position estimation error is produced, which affects the control performance of sensorless PMSM drives [14], [15].

The rotor position information can also be obtained by observing the rotor flux, which is aligned with the direction of the permanent magnet pole. The rotor flux changes relatively small with different working conditions and this method has good estimation performance over a wider speed operation range [16]. Since the flux information is usually obtained by integrating the EMF, the initial value setting and the dc bias of EMF can cause saturation of the integrator. To solve this issue, a high-pass filter (HPF) was adopted before the integrator to filter out the dc bias [17]. The combination of HPF and pure integral in series can be modified as a first-order low-pass filter (LPF). However, the adopted filter causes the amplitude attenuation and phase shift of the estimated rotor flux, leading to an estimation error in the rotor position. In [18], the estimated rotor flux error was directly compensated based on the frequency characteristic of the LPF. In [19], a compensation strategy based on the linear extended state observer in the estimated synchronous rotating reference frame was proposed to deal with the dc bias. A disturbance observer can be adopted to eliminate the dc bias [20] but increases the complexity of the flux observer.

Manuscript received 11 April 2023; revised 25 July 2023; accepted 2 September 2023. Date of publication 11 September 2023; date of current version 23 October 2023. This work was supported by the Research Fund for the National Natural Science Foundation of China under Grants 52125701, 52307048, and 52177034. Recommended for publication by Associate Editor K. Akatsu. *(Corresponding author: Dawei Ding.)*

The authors are with the School of Electrical Engineering and Automation, Harbin Institute of Technology, Harbin 150001, China (e-mail: 21b906039@stu.hit.edu.cn; dingdawei@hit.edu.cn; zhgq@hit.edu.cn; li_binxing@163.com; wqw0543@163.com; wgl818@hit.edu.cn; xudiang@hit.edu.cn).

Color versions of one or more figures in this article are available at https://doi.org/10.1109/TPEL.2023.3314009.

Digital Object Identifier 10.1109/TPEL.2023.3314009

The second-order generalized integrator (SOGI) has been a popular method due to the higher flexibility. Recently, researchers introduced the SOGI into the PMSM flux observer, replacing the first-order integrator [21]. The SOGI frequency locked loop (SOGI-FLL) was proposed in [22], which achieves adaptive tracking of the center frequency. In [23], a PMSM position observer based on SOGI was proposed. The theoretical analysis proved that the SOGI can eliminate the dc and the harmonic components in the estimated rotor flux. A third-order generalized integrator (TOGI) was proposed in [24], which can further enhance the suppression ability for the dc bias and the harmonic of flux observer. In [25], a cascaded SOGI that observes and suppresses the 5th and 7th harmonic introduced by the dead zone separately was proposed. As a whole, the SOGI-based methods can suppress the dc bias and the harmonic in the estimated rotor flux. However, the SOGI-based flux observers rarely consider the position estimation error caused by parameter mismatch. Additionally, compared with the linear oscillator, the nonlinear oscillator of the SOGI can enhance the robustness of the flux observer for sensorless PMSM drives.

This article proposes a flux observer based on an enhanced SOGI with a limit cycle oscillator (SOGI-LCO), aiming to improve the robustness of the model-based sensorless PMSM drive. By analyzing the disturbance caused by motor parameter mismatch, the proposed method introduces a nonlinear oscillator structure and restricts the rotating trajectory of the stator flux in an ideal state. The LCO with self-excited oscillation function can suppress the disturbance caused by motor parameter mismatch and reduce position estimation error. Based on the analysis of convergence, the parameter tuning of the proposed method is investigated. Moreover, the LCO structure can further optimize the suppression capability of SOGI algorithm for harmonic components, which enhances the robustness of the PMSM flux observer. The effectiveness of the proposed method is verified by experiments on a 2.2-kW PMSM platform.

II. Limitation of SOGI-Based PMSM Flux Observer

A. Flux Observer Based on SOGI

The voltage equation in the rotary reference frames (d–q axes) of PMSM can be expressed as

$$\begin{bmatrix} u_{\mathrm{sd}} \\ u_{\mathrm{sq}} \end{bmatrix} = \begin{bmatrix} R_{\mathrm{s}} + pL_{\mathrm{d}} & -\omega_{\mathrm{e}} L_{\mathrm{q}} \\ \omega_{\mathrm{e}} L_{\mathrm{d}} & R_{\mathrm{s}} + pL_{\mathrm{q}} \end{bmatrix} \begin{bmatrix} i_{\mathrm{sd}} \\ i_{\mathrm{sq}} \end{bmatrix} + \begin{bmatrix} 0 \\ \omega_{\mathrm{e}} \psi_{\mathrm{m}} \end{bmatrix} \tag{1}$$

where u_{sd}, u_{sq}, i_{sd}, and i_{sq} are the d–q axes stator voltages and currents, respectively, L_{d} and L_{q} are the d–q axes inductances, R_{s} is the stator resistance, ω_{e} is the electrical speed, ψ_{m} is the flux of the permanent magnet, and p is the differential operator.

According to [26], the active flux can be defined as $\psi_{\mathrm{a}} = i_{\mathrm{sd}}(L_{\mathrm{d}}\text{-}L_{\mathrm{q}})+\psi_{\mathrm{m}}$. Substituting the active flux ψ_{a} into (1) and transforming to the stationary reference frames ($\alpha-\beta$ axes), the active flux of PMSM can be expressed as

$$\begin{bmatrix} \psi_{\mathrm{a}\boldsymbol{\alpha}} \\ \psi_{\mathrm{a}\boldsymbol{\beta}} \end{bmatrix} = \int \left(\begin{bmatrix} u_{\mathrm{s}\boldsymbol{\alpha}} \\ u_{\mathrm{s}\boldsymbol{\beta}} \end{bmatrix} - \begin{bmatrix} R_{\mathrm{s}} & 0 \\ 0 & R_{\mathrm{s}} \end{bmatrix} \begin{bmatrix} i_{\mathrm{s}\boldsymbol{\alpha}} \\ i_{\mathrm{s}\boldsymbol{\beta}} \end{bmatrix} \right) dt - \begin{bmatrix} L_{\mathrm{q}} i_{\mathrm{s}\boldsymbol{\alpha}} \\ L_{\mathrm{q}} i_{\mathrm{s}\boldsymbol{\beta}} \end{bmatrix} \tag{2}$$

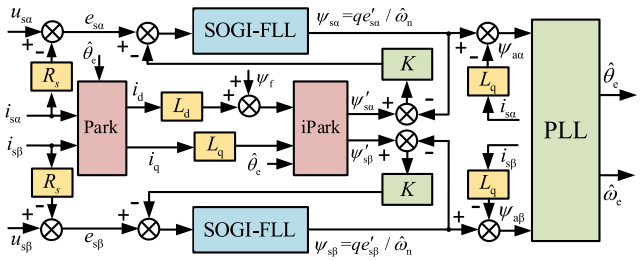

Fig. 1. Block diagrams of the conventional SOGI-based flux observer.

$$\theta_{\mathrm{e}} = \arctan\left(\frac{\psi_{\mathrm{a}\boldsymbol{\beta}}}{\psi_{\mathrm{a}\boldsymbol{\alpha}}}\right) \tag{3}$$

where $u_{\mathrm{s}\alpha}$, $u_{\mathrm{s}\beta}$, $i_{\mathrm{s}\alpha}$, $i_{\mathrm{s}\beta}$, $\psi_{\mathrm{a}\alpha}$, and $\psi_{\mathrm{a}\beta}$ are the $\alpha-\beta$ axes stator voltages, currents, and active fluxes, respectively, θ_{e} is the electrical angle. As the direction of ψ_{m} and i_{sd} are aligned, the direction of active flux is consistent with the d-axis. Then the rotor position can be obtained by observing the active flux.

It can be seen from (2) that the initial value setting of the integrator and the dc bias introduced by sampling error produce disturbances to the estimated active flux due to the use of first-order integrator. According to [21], an SOGI-based flux observer for sensorless PMSM drive has been adopted to address the issue, as shown in Fig. 1. Taking the α-axis as an example, the closed-loop transfer functions of SOGI-FLL between the stator EMF $e_{\mathrm{s}\alpha}$ and the filtering signal $e'_{\mathrm{s}\alpha}$, the quadrature signal $qe'_{\mathrm{s}\alpha}$ can be expressed as

$$\mathbf{D}(s) = \frac{e'_{\mathrm{s}\alpha}(s)}{e_{\mathrm{s}\alpha}(s)} = \frac{k\hat{\omega}_{\mathrm{n}} s}{s^2 + k\hat{\omega}_{\mathrm{n}} s + \hat{\omega}_{\mathrm{n}}^2} \tag{4}$$

$$\mathbf{Q}(s) = \frac{qe'_{\mathrm{s}\alpha}(s)}{e_{\mathrm{s}\alpha}(s)} = \frac{k\hat{\omega}_{\mathrm{n}}^2}{s^2 + k\hat{\omega}_{\mathrm{n}} s + \hat{\omega}_{\mathrm{n}}^2} \tag{5}$$

where the superscript "^" denotes the estimated value, $\hat{\omega}_{\mathrm{n}}$is the estimated center frequency, k is the error gain, $\boldsymbol{D}$(s) and $\boldsymbol{Q}$(s) are the transfer functions of the filtering section and the integration section, respectively.

The stator flux $\psi_{\mathrm{s}\alpha}$ can be obtained as $\psi_{\mathrm{s}\alpha}=qe'_{\mathrm{s}\alpha}/\hat{\omega}_{\mathrm{n}}$. The active flux $\psi_{\mathrm{a}\alpha}$ is related to the $\psi_{\mathrm{s}\alpha}$, which in turn affects the position estimation accuracy. Based on the phase relationship between the signal error ε and the quadrature signal $qe'_{\mathrm{s}\alpha}$, the frequency-locked loop is designed. The FLL achieves the adaptive tracking of $\hat{\omega}_{\mathrm{n}}$, enabling the algorithm to output the ideal filtering and integration result.

Assuming that the center frequency of the FLL is consistent with the fundamental frequency of the stator EMF. Combined with (4), the estimated α-axis stator flux $\hat{\psi}_{\mathrm{s}\boldsymbol{\alpha}}$ can be obtained as

$$\begin{aligned} \hat{\psi}_{\mathrm{s}\boldsymbol{\alpha}}(t) &= L^{-1}\left[\hat{\psi}_{\mathrm{s}\boldsymbol{\alpha}}(s)\right] = L^{-1}\left[\frac{1}{\omega_1}\cdot\mathbf{Q}(s)\cdot e_{\mathrm{s}\boldsymbol{\alpha}}(s)\right] \\ &= \frac{e_{\mathrm{s}\boldsymbol{\alpha}0}k}{\omega_1} + \frac{e_{\mathrm{s}\boldsymbol{\alpha}1}}{\omega_1}\sin\left(\omega_1 t + \varphi_1 - \frac{\pi}{2}\right) \\ &\quad + \sum_{\mathrm{i}=2}^{\infty}\left[\frac{\left(1-a_{\mathrm{i}}^2\right)^2}{k^2 a_{\mathrm{i}}^2} + 1\right]^{-\frac{1}{2}} \end{aligned}$$

$$\cdot \frac{e_{s\boldsymbol{\alpha}i}}{\omega_i} \sin\left[\omega_i t + \varphi_i - \frac{\pi}{2} + \tan^{-1}\left(\frac{\omega_1^2 - \omega_i^2}{\omega_1 \omega_i i}\right)\right] \tag{6}$$

where $L^{-1}()$ represents the inverse Laplace transform, $e_{s\alpha 0}$, $e_{s\alpha 1}$, and $e_{s\alpha i}$ represent the dc, the fundamental, and the ith ($i = 2, 3, 4\ldots$) harmonic components of $e_{s\alpha}$, respectively. ω_1 and ω_i represent the rotating angular velocities of the fundamental and the ith harmonic components of $e_{s\alpha}$, respectively. φ_1 and φ_i represent the phase values of the fundamental and the ith harmonic components of $e_{s\alpha}$, respectively. $a_i = \omega_i/\omega_1$ is the ratio of the harmonic frequency to the fundamental frequency.

It can be seen from (6) that the SOGI can integrate the fundamental component of the stator EMF without introducing additional phase lag or amplitude attenuation. Also, this method has a certain suppression effect on dc bias and harmonic distortion.

B. Disturbance Analysis of Parameter Mismatch

In the drive system, disturbances can cause perturbations in the input signals of the SOGI. Considering the influence of motor parameter mismatch, the impact of the disturbance on the flux observer is analyzed below.

According to the active flux shown in (2), the parameters such as R_s and L_q are needed in the observer. Considering the effect of motor parameter mismatch, the actual stator resistance and q-axis inductance can be represented as

$$\begin{cases} R'_s = R_s + \Delta R_s \\ L'_q = L_q + \Delta L_q \end{cases} \tag{7}$$

where R'_s, L'_q, ΔR_s, and ΔL_qrepresent the error value and actual value of the stator resistance and q-axis inductance, respectively.

According to [27], considering the closed-loop flux observer shown in Fig. 1, the estimation error of the stator flux is corrected in real time by the feedback gain K. The estimation error of EMF caused by parameter mismatch can be expressed as

$$\begin{aligned} \hat{e}_{s\boldsymbol{\alpha}} &= e_{s\boldsymbol{\alpha}1} \sin(\omega_1 t + \varphi_1) \\ &= e_{s\boldsymbol{\alpha}} - (\Delta R_s + j\omega_1 \Delta L_q)\, i_{s\boldsymbol{\alpha}} \end{aligned} \tag{8}$$

where j is the imaginary unit. It can be seen from (8) that parameter mismatch introduces an additional fundamental component disturbance in the estimation of stator EMF, which results in the rotor position error.

The control rate of the oscillator part of SOGI can be expressed as

$$\begin{cases} \dot{\hat{e}}_{s\boldsymbol{\alpha}} = -\omega_1 q\hat{e}'_{s\boldsymbol{\alpha}} \\ q\dot{\hat{e}}'_{s\boldsymbol{\alpha}} = \omega_1 \hat{e}'_{s\boldsymbol{\alpha}} \end{cases}. \tag{9}$$

As shown in (8), under the condition that the additional impedance appears in the estimation of the stator EMF, the math solution to (9) is

$$\begin{cases} \hat{e}'_{s\boldsymbol{\alpha}}(t) = (e_{s\boldsymbol{\alpha}1} + \Delta e_{s\boldsymbol{\alpha}1}) \sin(\omega_1 t_1) \\ q\hat{e}'_{s\boldsymbol{\alpha}}(t) = -(e_{s\boldsymbol{\alpha}1} + \Delta e_{s\boldsymbol{\alpha}1}) \cos(\omega_1 t) \end{cases}. \tag{10}$$

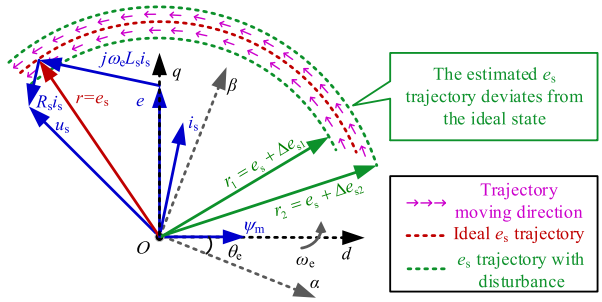

Fig. 2. Trajectory diagram of stator EMF with the SOGI method.

It can be seen from (10), the linear oscillator structure in SOGI is difficult to suppress the disturbance caused by the parameter mismatch. The trajectory of the stator EMF $\boldsymbol{e}_s$ in the stationary reference frames is circular in most cases. Based on (10), in the presence of disturbances $\Delta \mathbf{e}_{s1}$ and $\Delta \mathbf{e}_{s2}$, the $\boldsymbol{e}_s$ moving trajectory adopting SOGI method is shown in Fig. 2.

It can be seen that the SOGI cannot ensure that the estimated variable converges to an unchanged state when there is a fundamental component disturbance in the input signal. Therefore, the SOGI-based PMSM flux observer has unsatisfactory robustness to motor parameter mismatch.

III. Proposed Flux Observer Based on SOGI-LCO

A. Principle of the Proposed Flux Observer

If a constraint is imposed on the estimated stator EMF trajectory in Fig. 2 with the direction of its rotation, the stator flux trajectory will converge to the expected state. Then the disturbance caused by parameter mismatch can be suppressed. In order to improve the disturbance suppression ability of SOGI for the fundamental component of input disturbance caused by motor parameter mismatch, a flux observer based on SOGI-LCO for sensorless PMSM drive is proposed, as shown in Fig. 3. In the two-dimensional (2-D) nonlinear systems, there is a limit cycle system that simulates self-sustaining spontaneous phenomena of self-excited oscillations. The system can maintain oscillation even in the absence of external surrounding forcing. The LCO can converge to its set closed trajectory under any external disturbances and has good disturbance rejection performance [28].

The LCO is capable of maintaining the stable periodic motion of the stator EMF trajectory, without being affected by the disturbance caused by parameter mismatch. Taking the α-axis as an example, the equation for LCO is

$$\begin{cases} \dot{r} = -r(r^2 - A_0^2) \\ r = e_{s\alpha} \\ \dot{\theta} = \hat{\omega}_n \end{cases} \tag{11}$$

where r is the oscillation radius of $e_{s\alpha}$, θ is the rotation angle, and A_0 is the convergence radius.

Based on the first formula in (11), Fig. 4 shows the characteristic curve of the oscillator in the coordinate frame with the $e_{s\alpha}$ as the abscissa and $\dot{e}_{s\alpha}$ as the ordinate. It can be seen that the oscillator has three equilibrium states: the equilibrium point

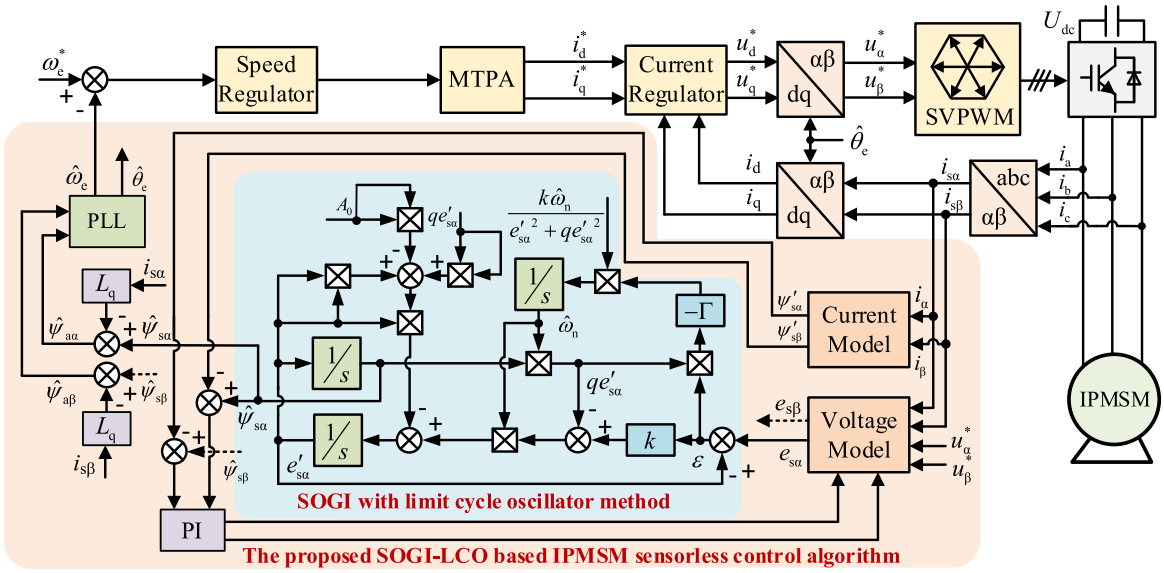

Fig. 3. Proposed flux observer based on SOGI-LCO for sensorless PMSM drive.

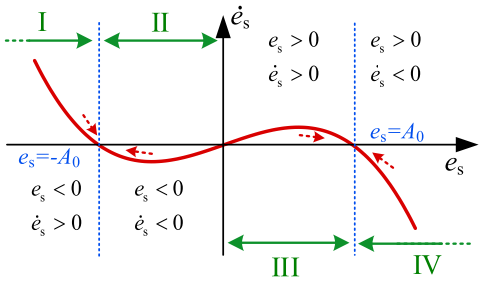

Fig. 4. Characteristic curve of LCO.

when $e_{s\alpha}=0$, the equilibrium rotating closed trajectory $e_{s\alpha}=$ -A_0 when $e_{s\alpha}$ is in Regions I and II, and the equilibrium rotating closed trajectory $e_{s\alpha}=A_0$ when $e_{s\alpha}$ is in Regions III and IV. All other unstable states will converge to the equilibrium states.

By substituting the transformation relationship of the controller output signal as $e'_{s\alpha}=e_{s\alpha}\cos\theta$ and $qe'_{s\alpha}=e_{s\alpha}\sin\theta$ into (11), the control law of the oscillator can be obtained as

$$\begin{cases} \dot{e}'_{s\alpha}=-\hat{\omega}_n qe'_{s\alpha}-e'_{s\alpha}(e'^2_{s\alpha}+qe'^2_{s\alpha}-A_0^2) \\ q\dot{e}'_{s\alpha}=\hat{\omega}_n e'_{s\alpha} \\ \psi_{s\alpha}=qe'_{s\alpha}/\hat{\omega}_n \end{cases}. \tag{12}$$

In combination with the SOGI algorithm, the control law of the proposed method can be represented as

$$\begin{cases} s\dot{e}'_{s\alpha}=\hat{\omega}_n\left[\varepsilon k\left(e_{s\alpha}-e'_{s\alpha}\right)-1qe'_{s\alpha}\right]-e'_{s\alpha}(e'^2_{s\alpha}+qe'^2_{s\alpha}-A_0^2) \\ s\dot{\hat{\omega}}_n=-\Gamma\varepsilon qe'_{s\alpha}\cdot\frac{k\hat{\omega}_n}{e'^2_{s\alpha}+qe'^2_{s\alpha}} \\ q\dot{e}'_{s\alpha}=\hat{\omega}_n e'_{s\alpha} \\ \psi_{s\alpha}=qe'_{s\alpha}/\hat{\omega}_n \end{cases} \tag{13}$$

where Γ is the gain of FLL, and ε is the error signal.

B. Convergence Analysis and Parameter Design

Based on the previous analysis, the convergence of the three equilibrium states of the oscillator is analyzed below.

1) Equilibrium Point at $e_{s\alpha}=0$*:* The equilibrium point has $e'_{s\alpha}=0$ and $qe'_{s\alpha}=0$. The state equation can be expressed as

$$\begin{bmatrix} \dot{e}'_{s\alpha} \\ q\dot{e}'_{s\alpha} \end{bmatrix}=\begin{bmatrix} A_0^2 & -\hat{\omega}_n \\ \hat{\omega}_n & 0 \end{bmatrix}\cdot\begin{bmatrix} e'_{s\alpha} \\ qe'_{s\alpha} \end{bmatrix}. \tag{14}$$

According to (14), the characteristic values λ_1 and λ_2 can be obtained as

$$\lambda_{1,2}=\left|\lambda I-\begin{bmatrix} A_0^2 & -\hat{\omega}_n \\ \hat{\omega}_n & 0 \end{bmatrix}\right|=\frac{A_0^2\pm\sqrt{A_0^4-4\hat{\omega}_n^2}}{2}. \tag{15}$$

It can be seen from (15) that the real part of the characteristic values is always positive. The oscillator diverges at $e_{s\alpha}=0$.

2) Equilibrium Trajectory at $e_{s\alpha}=\pm A_0$*:* Adopting the form of the Lyapunov function can only prove that the observer converges to a certain point. It is impossible to prove that the observer converges to a closed trajectory. Differentiating (11) and transforming it into the form of the Liénard equation:

$$\ddot{e}_{s\alpha}+\left(3e_{s\alpha}^2-A_0^2\right)\dot{e}_{s\alpha}=0 \tag{16}$$

where $f(e_{s\alpha})=3e_{s\alpha}^2-A_0^2$ is the damping function.

According to the Liénard theorem.

a) $e_{s\alpha}, f(e_{s\alpha})$ are continuously differentiable.

b) $\forall e_{s\alpha}\in\boldsymbol{R}, f(-e_{s\alpha})=f(e_{s\alpha})$.

c) Construct a function $F(x)$ where

$$F(x)=\int_0^x f(e_{s\alpha})de_{s\alpha}=x^3-A_0^2x. \tag{17}$$

It can be seen from (17) that $F(x)<0$ when $0<x<A_0$. When $x>A_0$, $F(x)>0$ and $F(x)$ is nondecreasing. Also, there exists $\lim_{x\to+\infty}F(x)=+\infty$.

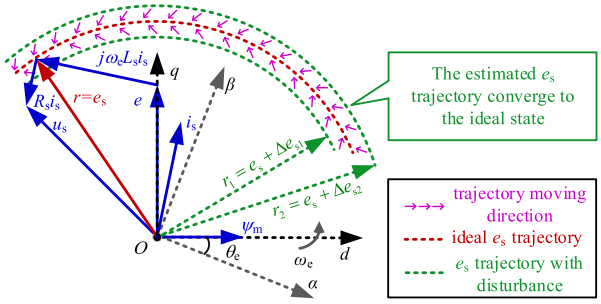

Fig. 5. Trajectory diagram of stator EMF with the proposed method.

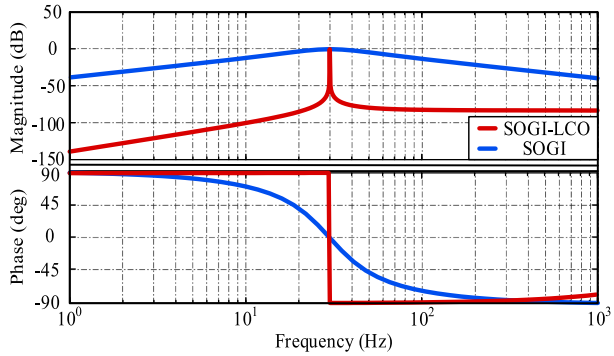

Fig. 6. Bode diagrams of the SOGI and the proposed method.

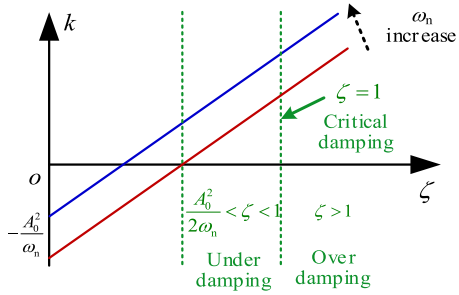

Fig. 7. Matched curves of k at different speeds.

According to criteria a, b, and c, it can be proved that the oscillator has a unique stable limit cycle around the origin in the phase plane. Since $e_{s\alpha} = -A_0$ has no practical meaning in the polar coordinate plane, the oscillator converges to the trajectory of $e_{s\alpha} = A_0$.

The vector relationship of the proposed algorithm is shown in Fig. 5. By adopting the proposed method, the errors caused by parameter mismatch in the stator flux can be limited to the expected trajectory, which can improve the robustness of the sensorless PMSM drive.

In order to compare the suppression capabilities of the proposed algorithm and the traditional SOGI algorithm for harmonic components, it is necessary to construct the transfer function of the proposed method. Rearranging (13), the result can be obtained as

$$k\hat{\omega}_n e_{s\alpha} = \left(k\hat{\omega}_n + A_0^2 + s + \frac{\hat{\omega}_n^2}{s}\right) e'_{s\alpha} - \left(1 + \frac{\hat{\omega}_n^2}{s^2}\right) e'^3_{s\alpha}. \tag{18}$$

Using $e'^3_{s\alpha} = 3e'^2_{s\alpha 0} e'_{s\alpha}$ to locally linearize (18), the closed-loop transfer functions between the stator EMF $e_{s\alpha}$ and the filtering signal $e'_{s\alpha}$, the quadrature signal $qe'_{s\alpha}$ can be expressed as

$$\mathbf{D}(s) = \frac{e'_{s\alpha}(s)}{e_{s\alpha}(s)} = \frac{k\hat{\omega}_n s^2}{s^3 + \left(k\hat{\omega}_n + A_0^2 - 3e'^2_{s\alpha 0}\right) s'^2 + \hat{\omega}_n^2 s - 3\hat{\omega}_n^2 e'^2_{s\alpha 0}}, \tag{19}$$

$$\mathbf{Q}(s) = \frac{qe'_{s\alpha}(s)}{e_{s\alpha}(s)} = \frac{k\hat{\omega}_n^2 s}{s^3 + \left(k\hat{\omega}_n + A_0^2 - 3e'^2_{s\alpha 0}\right) s^2 + \hat{\omega}_n^2 s - 3\hat{\omega}_n^2 e'^2_{s\alpha 0}} \tag{20}$$

where $e'_{s\alpha 0}$ is the DC component of $e'_{s\alpha}$.

According to (4) and (19), the frequency response characteristics of the traditional SOGI and the proposed method are shown in Fig. 6. Based on the experimental drive system, the center frequency is set to 60π rad/s, k is set to 1.414, and A_0 is set to 1. It can be seen from Fig. 6 that the proposed method has better suppression capabilities for the dc bias and harmonics than the traditional SOGI method.

Setting the denominator polynomial of (19) to 0 and ignoring the dc component introduced by the linearization process, the system characteristic equation can be obtained as

$$\begin{cases} s^2 + \left(k\omega_n + A_0^2\right) s + \omega_n^2 = 0 \\ k = \frac{2\zeta\omega_n - A_0^2}{\omega_n} \end{cases} \tag{21}$$

where ζ is the damping coefficient. Based on (21), the theoretical design curves of k under different speeds and damping ratios can be shown in Fig. 7. In order to ensure the algorithm has satisfactory dynamic performance, the damping coefficient should be set near the critical damping area ($\zeta = 1$).

According to (13), the frequency error signal ε_f can be expressed as

$$\varepsilon_f = \hat{\omega}_n \psi_{s\alpha} \left(e_{s\alpha} - e'_{s\alpha}\right) = \frac{\psi_{s\alpha}^2}{k} \left(\hat{\omega}_n^2 - \omega_n^2\right). \tag{22}$$

In the steady state, $(\hat{\omega}_n^2 - \omega_n^2)$ can be approximately equivalent to $2\hat{\omega}_n(\hat{\omega}_n - \omega_n)$. The dynamic tracking performance of the FLL can be expressed as

$$\dot{\hat{\omega}}_n = -\Gamma\varepsilon_f \approx -2\frac{\Gamma}{k}\psi_{s\alpha}^2 \hat{\omega}_n \left(\hat{\omega}_n - \omega_n\right). \tag{23}$$

Substituting (6) into (23), and ignoring the fluctuation frequency component, (24) can be obtained as

$$\dot{\hat{\omega}}_n = -\frac{\Gamma e_{s\alpha 1}^2}{k\hat{\omega}_n} \left(\hat{\omega}_n - \omega_n\right). \tag{24}$$

According to (24), the FLL can be simplified into a first-order feedback system:

$$\begin{cases} \mathbf{G_{FLL}}(s) = \frac{\Gamma}{s+\Gamma} \\ k_{\text{nor}} = \frac{k\hat{\omega}_{\text{n}}}{e^2_{\text{s}\alpha 1}} = \frac{k\hat{\omega}_{\text{n}}}{e'^2_{\text{s}\alpha} + qe'^2_{\text{s}\alpha}} \end{cases} \tag{25}$$

where $\boldsymbol{G}_{\mathbf{FLL}}(s)$ and k_{nor} are the transfer function and the normalized gain coefficient of FLL, respectively.

The theoretical value of the FLL gain coefficient can be obtained by designing the FLL time constant t_{sFLL}

$$\Gamma = \frac{5}{t_{\text{sFLL}}}. \tag{26}$$

C. Analysis of Disturbance Suppression Capability

The disturbance components of each frequency of the stator EMF are equivalent to the polar coordinate frame (x–y axes) as

$$\begin{cases} e_{\text{s}\alpha\_\text{x}} = e_{\text{s}\alpha 0}\cos\theta_{\text{es}\alpha 0} + e_{\text{s}\alpha 1}\cos\theta_{\text{es}\alpha 1} + \sum_{i=2}^{\infty} e_{\text{s}\alpha\text{i}}\cos\theta_{\text{es}\alpha\text{i}} \\ e_{\text{s}\alpha\_\text{y}} = e_{\text{s}\alpha 0}\sin\theta_{\text{es}\alpha 0} + e_{\text{s}\alpha 1}\sin\theta_{\text{es}\alpha 1} + \sum_{i=2}^{\infty} e_{\text{s}\alpha\text{i}}\cos\theta_{\text{es}\alpha\text{i}} \end{cases} \tag{27}$$

where $e_{\text{s}\alpha\text{·x}}$ and $e_{\text{s}\alpha\text{·y}}$ are the x-axis and y-axis components of the stator EMF, respectively. $\theta_{\text{es}\alpha 0}$, $\theta_{\text{es}\alpha 1}$, and $\theta_{\text{es}\alpha\text{i}}$ are the angular coordinates of the dc, the fundamental, and the ith harmonic components of the stator EMF, respectively. It should be noted that the dc component $e_{\text{s}\alpha 0}$ is a point in the polar coordinate system. So, in (27), $e_{\text{s}\alpha 0}$ and $\theta_{\text{es}\alpha 0}$ are constants. The derivatives with respect to time and length are both 0.

For the dc component, the relationship is

$$\begin{cases} e_{\text{s}\alpha 0\_\text{x}} = e_{\text{s}\alpha 0}\cos\theta_{\text{es}\alpha 0}, e_{\text{s}\alpha 0\_\text{y}} = e_{\text{s}\alpha 0}\sin\theta_{\text{es}\alpha 0} \\ \dot{e}_{\text{s}\alpha 0} = \dot{\theta}_{\text{es}\alpha 0} = 0, \dot{e}_{\text{s}\alpha 0\_\text{x}} = 0, \dot{e}_{\text{s}\alpha 0\_\text{x}} = 0 \end{cases} \tag{28}$$

where $e_{\text{s}\alpha 0\text{·x}}$ and $e_{\text{s}\alpha 0\text{·y}}$ are the x-axis and y-axis components of the dc disturbance of the stator EMF, respectively. Substituting (28) into (13), the results can be obtained as

$$\begin{cases} 0 = -\omega_1 e_{\text{s}\alpha 0}\sin\theta_{\text{es}\alpha 0} - e_{\text{s}\alpha 0}\cos\theta_{\text{es}\alpha 0}\left(e^2_{\text{s}\alpha 0} - A_0^2\right) \\ 0 = \omega_1 e_{\text{s}\alpha 0}\cos\theta_{\text{es}\alpha 0} \end{cases}. \tag{29}$$

The solution $e_{\text{s}\alpha 0} = 0$ of (29) can be expressed as the dc harmonic component of the stator EMF approaches to 0 in the steady state. That is, the proposed algorithm has a preferable suppression effect on the dc bias theoretically.

For the HF disturbance component of the stator EMF, the relationship can be expressed as

$$\begin{cases} e_{\text{s}\alpha\text{h}\_\text{x}} = \sum_{i=2}^{\infty} e_{\text{s}\alpha\text{i}}\cos\theta_{\text{es}\alpha\text{i}}, e_{\text{s}\alpha\text{h}\_\text{y}} = \sum_{i=2}^{\infty} e_{\text{s}\alpha\text{i}}\sin\theta_{\text{es}\alpha\text{i}} \\ \dot{e}_{\text{s}\alpha\text{h}\_\text{x}} = \sum_{i=2}^{\infty} \dot{e}_{\text{s}\alpha\text{i}}\cos\theta_{\text{es}\alpha\text{i}} - \sum_{i=2}^{\infty} \omega_{\text{i}} e_{\text{s}\alpha\text{i}}\sin\theta_{\text{es}\alpha\text{i}} \\ \dot{e}_{\text{s}\alpha\text{h}\_\text{y}} = \sum_{i=2}^{\infty} \dot{e}_{\text{s}\alpha\text{i}}\sin\theta_{\text{es}\alpha\text{i}} + \sum_{i=2}^{\infty} \omega_{\text{i}} e_{\text{s}\alpha\text{i}}\cos\theta_{\text{es}\alpha\text{i}} \end{cases} \tag{30}$$

where $e_{\text{s}\alpha\text{h·x}}$ and $e_{\text{s}\alpha\text{h·y}}$ are the sum of the x-axis and the y-axis HF disturbance components of the stator EMF, respectively.

Substituting (30) into (13), the following can be obtained:

$$\begin{cases} \sum_{i=2}^{\infty} \dot{e}_{\text{s}\alpha\text{i}} = \sum_{i=2}^{\infty} e_{\text{s}\alpha\text{i}}\left[(\omega_{\text{i}} - \omega_1)\tan\theta_{\text{es}\alpha\text{i}} - \left(r^2_{\text{es}\alpha\text{i}} - A_0^2\right)\right] \\ \sum_{i=2}^{\infty} \dot{e}_{\text{s}\alpha\text{i}} = \sum_{i=2}^{\infty} e_{\text{s}\alpha\text{i}}\left(\omega_1 - \omega_{\text{i}}\right)\tan^{-1}\theta_{\text{es}\alpha\text{i}} \end{cases}. \tag{31}$$

It can be seen from (31), there contains two dimensions: the radius dimension and the angle dimension of the harmonic components. Two dimensions are independent of each other. In order to analyze the convergence characteristics of the harmonic components radius dimension, combined with the first formula of (31), and integrated the angle over one limit cycle period, (32) can be obtained as

$$\begin{aligned} &\int_0^{2\pi} \sum_{i=2}^{\infty} \dot{e}_{\text{s}\alpha\text{i}} d\theta_{\text{es}\alpha\text{i}} \\ &= \int_0^{2\pi} \sum_{i=2}^{\infty} e_{\text{s}\alpha\text{i}}\left[(\omega_{\text{i}} - \omega_1)\tan\theta_{\text{es}\alpha\text{i}} - \left(e^2_{\text{s}\alpha\text{i}} - A_0^2\right)\right] d\theta_{\text{es}\alpha\text{i}}. \end{aligned} \tag{32}$$

Simplifying (32), the convergence of the proposed algorithm to the radius of harmonic components can be obtained as

$$\sum_{i=2}^{\infty} \dot{e}_{\text{s}\alpha\text{i}} = -\sum_{i=2}^{\infty} e_{\text{s}\alpha\text{i}}\left(e^2_{\text{s}\alpha\text{i}} - A_0^2\right). \tag{33}$$

For the ith ($i = 2, 3, 4\ldots$) harmonic, differentiating (33) and transforming it into the form of the Liénard equation:

$$\ddot{e}_{\text{s}\alpha\text{i}} + \left(3e^2_{\text{s}\alpha\text{i}} - A_0^2\right)\dot{e}_{\text{s}\alpha\text{i}} = 0 \tag{34}$$

where $f(e_{\text{s}\alpha\text{i}}) = 3e^2_{\text{s}\alpha\text{i}} - A_0^2$ is the damping function.

According to the Liénard theorem.

a) $e_{\text{s}\alpha\text{i}}$ and $f(e_{\text{s}\alpha\text{i}})$ are continuously differentiable.

b) $\forall e_{\text{s}\alpha\text{i}} \in \mathbf{R}, f(-e_{\text{s}\alpha\text{i}}) = f(e_{\text{s}\alpha\text{i}})$.

c) Construct a function $F(x)$ where

$$F(x) = \int_0^x f(e_{\text{s}\alpha\text{i}}) de_{\text{s}\alpha\text{i}} = x^3 - A_0^2 x. \tag{35}$$

It can be seen from (35) that $F(x)<0$ when $0<x<A_0$. When $x>A_0$, $F(x)>0$ and $F(x)$ is nondecreasing. Also, there exists $\lim_{x\to+\infty} F(x) = +\infty$.

According to criteria a, b, and c, it can be proved that the oscillator has a unique stable limit cycle around the origin in the phase plane. Since $e_{\text{s}\alpha\text{i}} = -A_0$ has no practical meaning in the polar coordinate plane, the oscillator converges to the trajectory of $e_{\text{s}\alpha\text{i}} = A_0$. Substituting $e_{\text{s}\alpha\text{i}} = A_0$ into the second formula of (31), the results can be obtained as

$$\sum_{i=2}^{\infty} \dot{e}_{\text{s}\alpha\text{i}} = A_0 \sum_{i=2}^{\infty} (\omega_1 - \omega_{\text{i}})\tan^{-1}\theta_{\text{es}\alpha\text{i}}. \tag{36}$$

According to (36), Fig. 8 shows the convergence pattern of $e_{\text{s}\alpha\text{i}}$. Since ω_{i} is $i(i = 23,4\ldots)$ times the frequency of ω_1, $e_{\text{s}\alpha\text{i}}$ will eventually converge to $e_{\text{s}\alpha\text{i}} = A_0$ trajectory and the proposed method has the effect of suppressing harmonic disturbances in theory.

Summarizing the above analysis, the proposed method improves the ability of the flux observer to suppress the dc bias and the harmonics. Table I summarizes the comparison of the antidisturbance ability of the proposed method and the SOGI method.

Fig. 9 shows the comparison between the SOGI and the proposed method on the harmonic suppression ability. It can be seen that the harmonic suppression ability of the SOGI

TABLE I
COMPARISON OF ANTIDISTURBANCE PERFORMANCE OF THE TWO METHODS

Method	DC bias	Fundamental wave	Harmonics	Fundamental disturbance
SOGI	$\frac{e_{s\alpha 0}k}{\omega_1}$	$\frac{e_{s\alpha 1}}{\omega_1}\sin\left(\omega_1 t+\varphi_1-\frac{\pi}{2}\right)$	$\sum_{i=2}^{\infty}\left[\frac{\left(1-a_i^2\right)^2}{k^2a_i^2}+1\right]^{-0.5}\cdot\frac{e_{s\alpha i}}{\omega_i}$	$\frac{e_{s\alpha 1}+\Delta e_{s\alpha 1}}{\omega_1}$
SOGI-LCO	0	$\frac{e_{s\alpha 1}}{\omega_1}\sin\left(\omega_1 t+\varphi_1-\frac{\pi}{2}\right)$	0	$\frac{e_{s\alpha 1}}{\omega_1}$

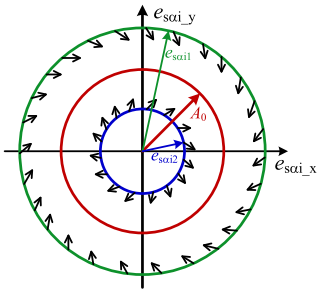

Fig. 8. Convergence pattern of *i*th stator EMF.

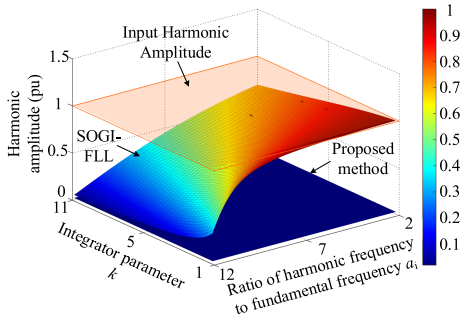

Fig. 9. Comparison of harmonic suppression ability between the SOGI and the proposed method.

method is affected by the k and the harmonic frequency. Near the fundamental frequency, the harmonic suppression ability of the proposed method is obviously better than that of SOGI method.

D. Analysis of Stability and Performance Comparison

According to Fig. 3, the simplified model of the proposed flux observer in the frequency domain is shown in Fig. 10.

The closed-loop transfer function of SOGI-LCO between the estimated stator EMF $\hat{e}_{s\alpha}$ and the filtered output signal $\hat{\psi}_{s\alpha}$can

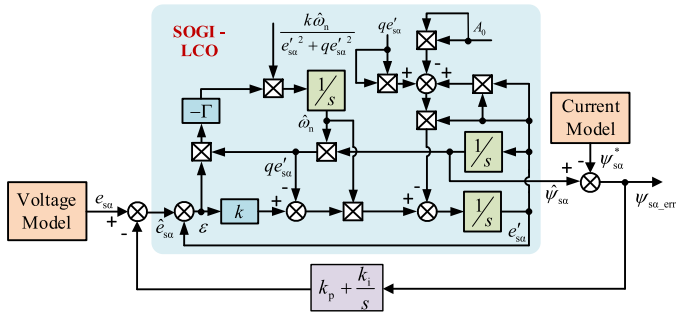

Fig. 10. Simplified block diagram of the proposed flux observer.

be expressed as

$$G_{\mathrm{SOGI\_LCO}}(s)=\frac{\hat{\psi}_{s\alpha}(s)}{\hat{e}_{s\alpha}(s)}=\frac{k\hat{\omega}_{\mathrm{n}}s}{s^3+\left(k\hat{\omega}_{\mathrm{n}}+A_0^2-3e_{s\alpha 0}'^2\right)s^2+\hat{\omega}_{\mathrm{n}}^2s-3\hat{\omega}_{\mathrm{n}}^2e_{s\alpha 0}'^2}. \quad (37)$$

Then, the system closed-loop transfer function $G_{\mathrm{fluxob}}(s)$ in the frequency domain can be expressed as (38) shown at the bottom of this page, where $G_{\mathrm{PI}}(s)$ is the transfer function of PI controller in the feedback loop, k_{p} and k_{i} are the proportional and integral coefficients of PI controller, respectively.

In order to analyze the stability of the proposed flux observer, the pole-zero diagram can be obtained according to (38), as shown in Fig. 11. Based on the experimental drive system, the center frequency $\hat{\omega}_{\mathrm{n}}$ is set to 60π rad/s, k is set to 1.414, and A_0 is set to 1. As can be seen from Fig. 11, the poles of the closed-loop transfer function lie on the left half of the s-plane, which can verify the stability of the proposed flux observer. As k_{p} and k_{i} increase, the poles gradually move away from zero. Moreover, considering the effect of observer bandwidth, the selections of k_{p} and k_{i} should not be too large.

$$\begin{aligned}G_{\mathrm{fluxob}}(s)&=\frac{G_{\mathrm{SOGI\_LCO}}(s)}{1+G_{\mathrm{SOGI\_LCO}}(s)G_{\mathrm{PI}}(s)}\hat{e}_{s\alpha}(s)-\frac{1}{1+G_{\mathrm{SOGI\_LCO}}(s)G_{\mathrm{PI}}(s)}\hat{\psi}_{s\alpha}(s)\\&=\frac{k\hat{\omega}_{\mathrm{n}}s}{s^3+\left(k\hat{\omega}_{\mathrm{n}}+A_0^2-3e_{s\alpha 0}'^2\right)s^2+\left(\hat{\omega}_{\mathrm{n}}^2+kk_{\mathrm{p}}\hat{\omega}_{\mathrm{n}}\right)s-3\hat{\omega}_{\mathrm{n}}^2e_{s\alpha 0}'^2+kk_{\mathrm{i}}\hat{\omega}_{\mathrm{n}}}\hat{e}_{s\alpha}(s)\\&\quad-\frac{s^3+\left(k\hat{\omega}_{\mathrm{n}}+A_0^2-3e_{s\alpha 0}'^2\right)s^2+\hat{\omega}_{\mathrm{n}}^2s-3\hat{\omega}_{\mathrm{n}}^2e_{s\alpha 0}'^2}{s^3+\left(k\hat{\omega}_{\mathrm{n}}+A_0^2-3e_{s\alpha 0}'^2\right)s^2+\left(\hat{\omega}_{\mathrm{n}}^2+kk_{\mathrm{p}}\hat{\omega}_{\mathrm{n}}\right)s-3\hat{\omega}_{\mathrm{n}}^2e_{s\alpha 0}'^2+kk_{\mathrm{i}}\hat{\omega}_{\mathrm{n}}}\hat{\psi}_{s\alpha}(s)\end{aligned} \quad (38)$$

TABLE II
DIFFERENCE BETWEEN PROPOSED OBSERVER AND THE ADVANCED FLUX OBSERVERS

Methods	Observer equation	Remarks
Reduced-order flux observer [29]	$\begin{cases} \dfrac{d\hat{\psi}_{\mathrm{d}}}{dx} = u_{\mathrm{sd}} - R_{\mathrm{s}} i_{\mathrm{sd}} + \omega_e L_{\mathrm{q}} i_{\mathrm{sq}} + k_1\left(\hat{\psi}_{\mathrm{d}} - L_{\mathrm{sd}} i_{\mathrm{sd}} - \hat{\psi}_{\mathrm{m}}\right) \\ \dfrac{d\hat{\theta}_{\mathrm{e}}}{dx} = \dfrac{u_{\mathrm{sq}} - R_{\mathrm{s}} i_{\mathrm{sq}} - L_{\mathrm{q}} \dfrac{di_{\mathrm{sq}}}{dx} + k_2\left(\hat{\psi}_{\mathrm{d}} - L_{\mathrm{d}} i_{\mathrm{sd}} - \hat{\psi}_{\mathrm{m}}\right)}{\hat{\psi}_{\mathrm{d}}} \end{cases}$	- Excellent dynamic performance. - Excellent ultra-low-speed observation accuracy. - Simple structure and easy to implement. - Parameter design is complex.
Nonlinear flux observer [30]	$\begin{bmatrix} \psi_{\mathrm{s}\alpha} \\ \psi_{\mathrm{s}\beta} \end{bmatrix} = \int \left(\begin{bmatrix} u_{\mathrm{s}\alpha} \\ u_{\mathrm{s}\beta} \end{bmatrix} - \begin{bmatrix} R_{\mathrm{s}} & 0 \\ 0 & R_{\mathrm{s}} \end{bmatrix} \begin{bmatrix} i_{\mathrm{s}\alpha} \\ i_{\mathrm{s}\beta} \end{bmatrix} \right) dt + \frac{\lambda}{2} \hat{\psi}_{\mathrm{r}} \left[\hat{\psi}_{\mathrm{m}}^2 - \left| \hat{\psi}_{\mathrm{r}} \right|^2 \right]$	- Capable of tracking disturbance component. - Fast convergence of dynamic processes. - Excellent parameter robustness. - Weak ultra-low-speed observation accuracy.
Frequency-adaptive flux observer [31]	$\begin{cases} \begin{bmatrix} \psi_{\mathrm{sd}} \\ \psi_{\mathrm{sq}} \end{bmatrix} = \int \left(\begin{bmatrix} u_{\mathrm{sd}} \\ u_{\mathrm{sq}} \end{bmatrix} - \begin{bmatrix} R_{\mathrm{s}} & 0 \\ 0 & R_{\mathrm{s}} \end{bmatrix} \begin{bmatrix} i_{\mathrm{sd}} \\ i_{\mathrm{sq}} \end{bmatrix} \right) dt = \int \boldsymbol{v} dt \\ \boldsymbol{\psi}_{\mathrm{s}}(s) = \dfrac{2\zeta \left| \omega_{\mathrm{n}} \right|}{s^2 - 2\zeta \left| \omega_{\mathrm{n}} \right| \cdot s + \left| \omega_{\mathrm{n}} \right|^2} \cdot \boldsymbol{v}(s) \end{cases}$	- Simple structure and easy to implement. - Applicable for PMSM DTC/FOC with good general performance. - Require the speed sensor.
Proposed SOGI-LCO based flux observer	$\begin{cases} \begin{bmatrix} \psi_{\mathrm{a}\alpha} \\ \psi_{\mathrm{a}\beta} \end{bmatrix} = \int \left(\begin{bmatrix} u_{\mathrm{s}\alpha} \\ u_{\mathrm{s}\beta} \end{bmatrix} - \begin{bmatrix} R_{\mathrm{s}} & 0 \\ 0 & R_{\mathrm{s}} \end{bmatrix} \begin{bmatrix} i_{\mathrm{s}\alpha} \\ i_{\mathrm{s}\beta} \end{bmatrix} \right) dt - \begin{bmatrix} L_{\mathrm{q}} i_{\mathrm{s}\alpha} \\ L_{\mathrm{q}} i_{\mathrm{s}\beta} \end{bmatrix} = \hat{\boldsymbol{\psi}}_{\mathrm{s}} - L_{\mathrm{q}} \boldsymbol{i}_{\mathrm{s}} \\ \hat{\boldsymbol{\psi}}_{\mathrm{s}}(s) = \dfrac{k\hat{\omega}_{\mathrm{n}} s}{s^3 + \left(k\hat{\omega}_{\mathrm{n}} + A_0^2 - 3e_{\mathrm{s}0}'^2\right)s^2 + \hat{\omega}_{\mathrm{n}}^2 s - 3\hat{\omega}_{\mathrm{n}}^2 e_{\mathrm{s}0}'^2} \cdot \hat{\boldsymbol{e}}_{\mathrm{s}}(s) \end{cases}$	- Good suppression capability of DC bias and harmonic. - Reduce estimation error during parameter mismatch. - Adaptive tracking of the frequency of fundamental waves. - Applicable in the complete torque range

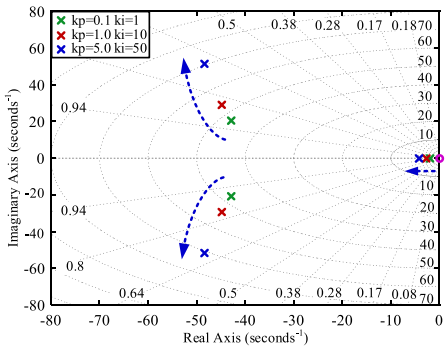

Fig. 11. Pole-zero diagram of the proposed flux observer.

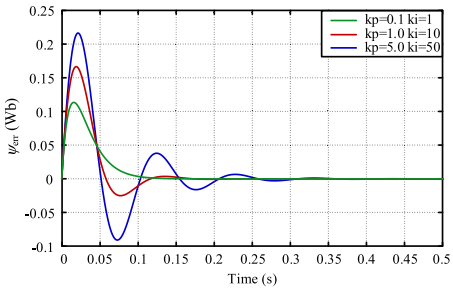

Fig. 12. Step response of the proposed flux observer.

To describe the difference between the proposed method and the existing advanced flux observer [29], [30], [31] more intuitively, a detailed comparison is listed in Table II.

Generally, the higher the order of the transfer function, the more complex the system performance analysis, the lower the controllability, and the more difficult the controller design. In order to verify the dynamic performance of the proposed algorithm, the step response between the input and output error signals is plotted in Fig. 12 according to (38). It can be seen that the selection of PI controller parameters is a key factor affecting the dynamic performance of the flux observer. The flux observer can be regarded as a LPF in which the harmonic disturbances other than flux information can be filtered out. In order to improve the system stability, PI controller parameters should not be chosen too large. Smaller PI controller parameters introduce a greater effect on dynamic performance than that introduced by raising the observer order.

IV. EXPERIMENTAL RESULTS

In order to verify the effectiveness of the proposed SOGI-LCO method, experiments were performed on the 2.2-kW PMSM platform shown in Fig. 13. The parameters of test PMSM are listed in Table III. The sensorless scheme is realized by an ARM STM32F103VCT6 chip. The PWM carrier frequency, the switching frequency, and the sampling frequency are all set as 6 kHz. The parameters of the proposed method are set as $k = 1.414$, $\Gamma = 1000$, and $A_0 = 1$.

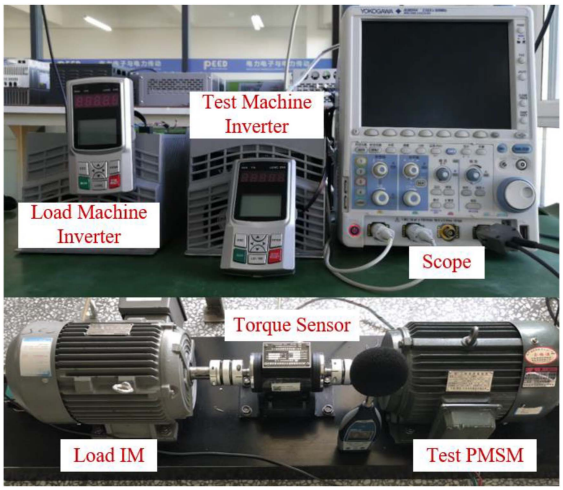

Fig. 13. Experimental platform of 2.2-kW PMSM.

TABLE III
EXPERIMENTAL PARAMETERS OF PMSM

Parameter	Value	Parameter	Value
Rated power	2.2 kW	Phase resistance	2.53 Ω
Rated voltage	380 V	D-axis inductance	22.38 mH
Rated current	5.6 A	Q-axis inductance	51.75 mH
Rated frequency	75 Hz	Pairs of poles	3
Rated torque	20 N·m	Magnetic flux	0.5 Wb

The experimental results of estimated variables fluctuation before and after adopting the proposed method are shown in Fig. 14 when the motor operates at 100 r/min and 100% rated load. It can be seen from Fig. 14(a) that the filtering effect of the proposed method is better than that of the SOGI method. Fig. 14(b) and (c) shows the 3-D Lissajous figures of the stator flux estimate result adopting the SOGI and the proposed algorithm, respectively. It can be seen that both algorithms have good filtering effects on dc bias. Fig. 14(d) and (e) shows the Fourier analysis of stator EMF before and after the enablement of the proposed method. Before enabling the proposed method, the amplitude of the 5th, 7th, and 11th harmonics are 0.042, 0.024, and 0.012 p.u., respectively. Compared to the traditional SOGI method, the proposed method has a better filtering effect on the harmonic disturbances in the stator EMF and flux.

Fig. 15 shows the experimental results of estimated variables fluctuation before and after adopting the proposed method in the presence of artificially added dc bias and harmonic disturbances in the input of the SOGI-LCO method when the motor operates at 100 r/min and 100% rated load. It can be seen from Fig. 15(a) that the dc bias and harmonic suppression effect are satisfied and the fluctuation of position estimation error is reduced after enabling the proposed algorithm. Fig. 15(b) and (c) shows the Fourier analysis of stator EMF before and after the enablement of the proposed method. Before enabling the proposed method, the amplitude of the 2nd, 3rd, 4th, and 5th harmonics are 0.095,

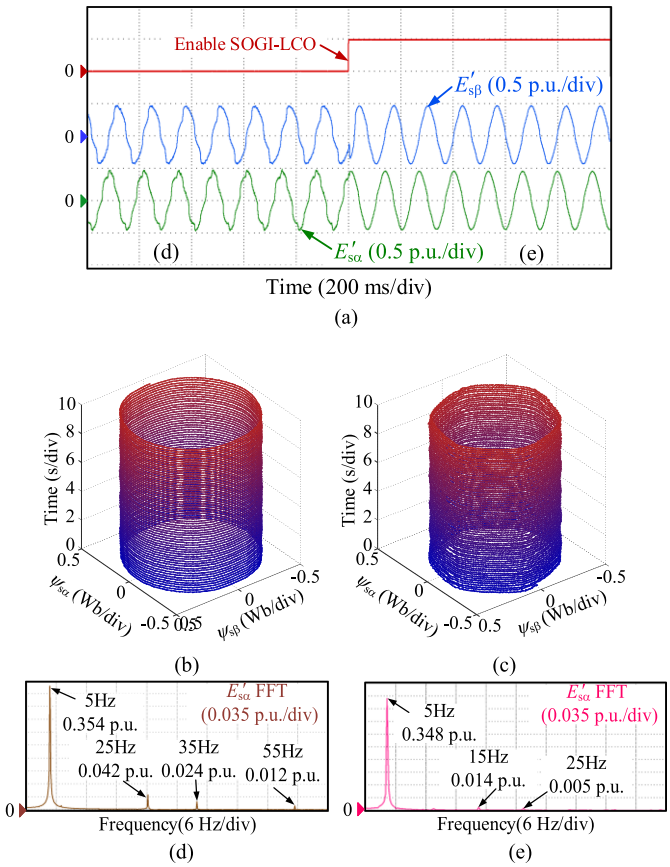

Fig. 14. Experimental results of the proposed method. (a) Comparison of the proposed method before and after enablement. (b) Flux estimates result with the SOGI method. (c) Flux estimates result with the proposed method. (d) FFT analysis of stator EMF before enablement. (e) FFT analysis of stator EMF after enablement.

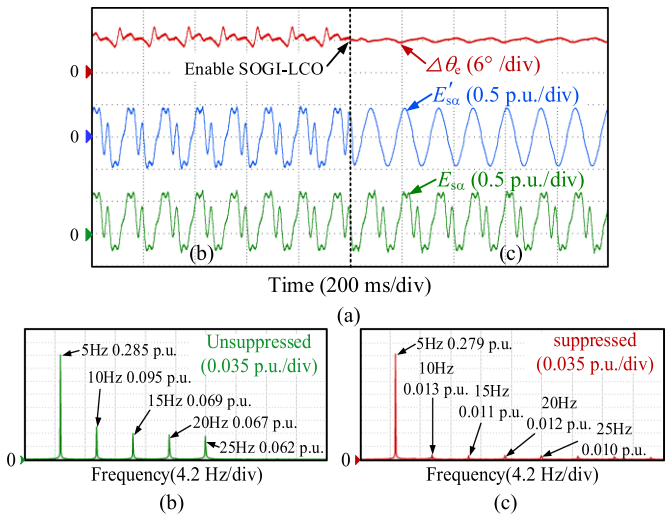

Fig. 15. Experimental results in the presence of artificially added dc bias and harmonic disturbances. (a) Comparison of the proposed method before and after enablement. (b) FFT analysis of stator EMF before enablement. (c) FFT analysis of stator EMF after enablement.

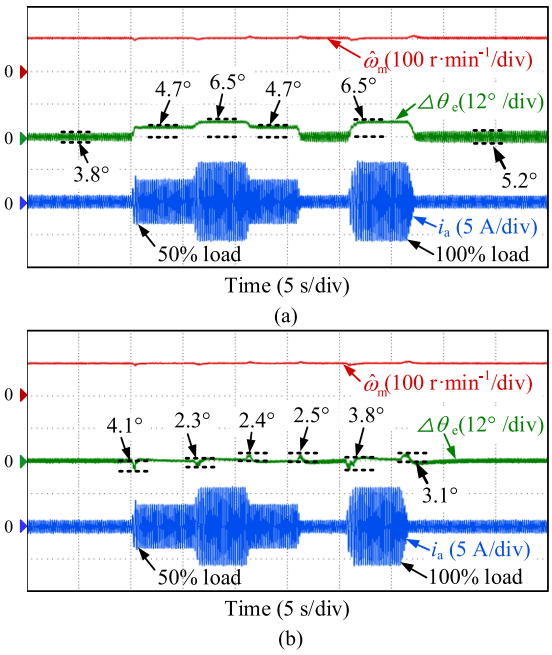

Fig. 16. Experimental results at 100 r/min operation speed under 100% rated load, 50% rated load, and no-load conditions. (a) SOGI. (b) SOGI-LCO.

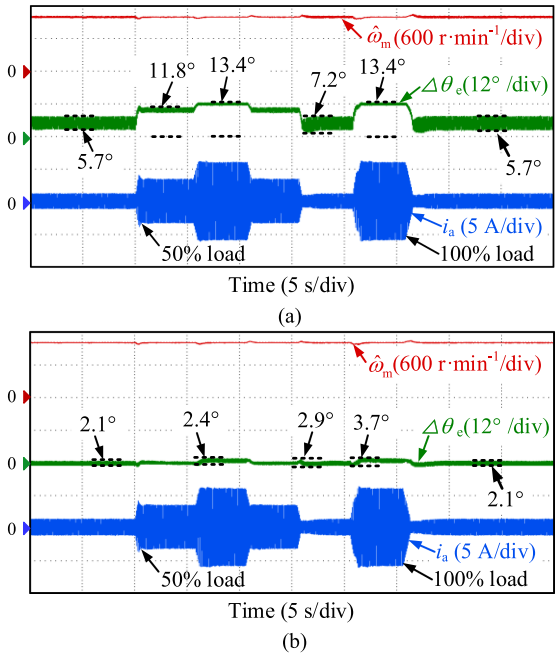

Fig. 17. Experimental results at 1000 r/min operation speed under 100% rated load, 50% rated load, and no-load conditions. (a) SOGI. (b) SOGI-LCO.

0.069, 0.067, and 0.062 p.u., respectively. Also, there are 0.2 p.u. dc bias in the input stator EMF. After enabling the proposed method, the dc bias is eliminated and the amplitude of the 2nd, 3rd, 4th, and 5th harmonics are reduced to 0.013, 0.011, 0.012, and 0.010 p.u., respectively. The proposed SOGI-LCO method is experimentally verified to have good suppression ability for the dc bias and harmonic disturbances.

Fig. 16 shows the experimental results of the speed and position estimation errors of the sensorless control using the SOGI and the proposed method when the motor operates at 100 r/min with load changes. As can be seen from Fig. 16(a) the maximum rotor position estimation error using the SOGI method is 6.5°, with a maximum fluctuation of 5.2°. In Fig. 16(b), the maximum rotor position estimation error using the proposed algorithm is 4.1°, and the static estimation error is close to zero. The position estimation performance of the proposed algorithm is better than that of the traditional method when the motor operates at 100 r/min.

Fig. 17 shows the experimental results of the speed and position estimation errors when the motor operates at 1000 r/min with load changes. It can be seen from Fig. 17(a) that the maximum rotor position estimation error adopting the SOGI method is 13.4°, with a maximum fluctuation of 5.7°. In Fig. 17(b), the maximum rotor position estimation error adopting the proposed method is 3.7°. Under the condition of 100% rated load, the maximum rotor position estimation error is 2.4°. The position estimation performance of the proposed method at a higher speed operation region is better than that of the traditional method.

Fig. 18 shows the experimental results of the speed and position estimation errors when the motor operates at 40 r/min (2.7% of rated speed) with load changes. It can be seen that the maximum rotor position estimation error adopting the proposed

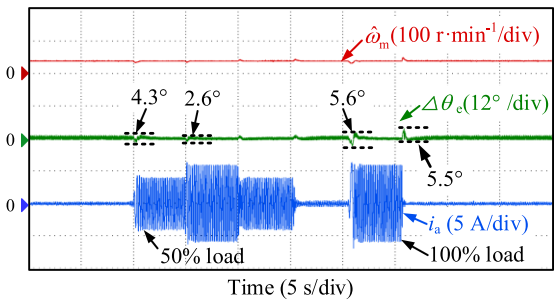

Fig. 18. Experimental results at 40 r/min operation speed under 100% rated load, 50% rated load, and no-load conditions.

method is 5.6°. Under the condition of 100% rated load, the maximum rotor position estimation error is 2.6°. The position estimation performance of the proposed method at ultra-low-speed region meets the normal operation requirements of PMSM.

The experimental comparison results between different methods are shown in Fig. 19 when the motor operates from 100 r/min to 1000 r/min. As can be seen from Fig. 19(a), the maximum rotor position estimation error at 1000 r/min is 5.8° by using the traditional SOGI method. In Fig. 19(b), the maximum rotor position estimation error is 4.4° with the proposed SOGI-LCO method, which has 19% reduction over the traditional method. Compared with the traditional method, the proposed method is more capable of suppressing the position estimation error during system dynamics.

Fig. 20 shows the experimental results of speed and position estimation error with the second-order SOGI-based method [32], the TOGI-based method [24], the ROGI-based method [33] and the proposed SOGI-LCO method under 1000 r/min

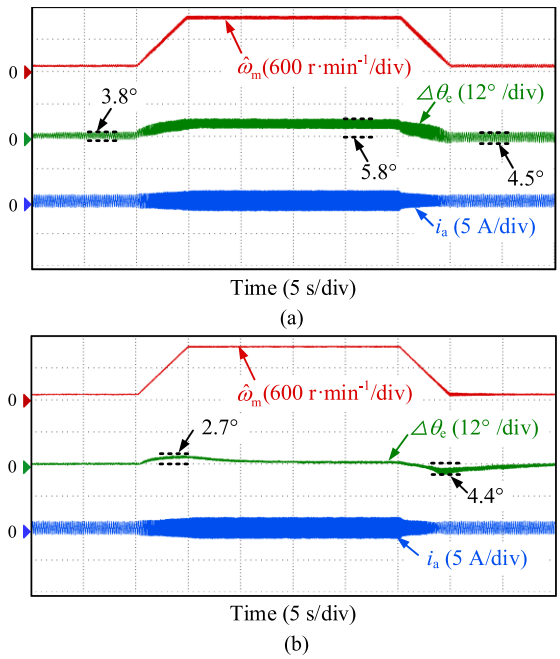

Fig. 19. Experimental comparison results of the speed fluctuation under the continuous speed variation conditions. (a) SOGI. (b) SOGI-LCO.

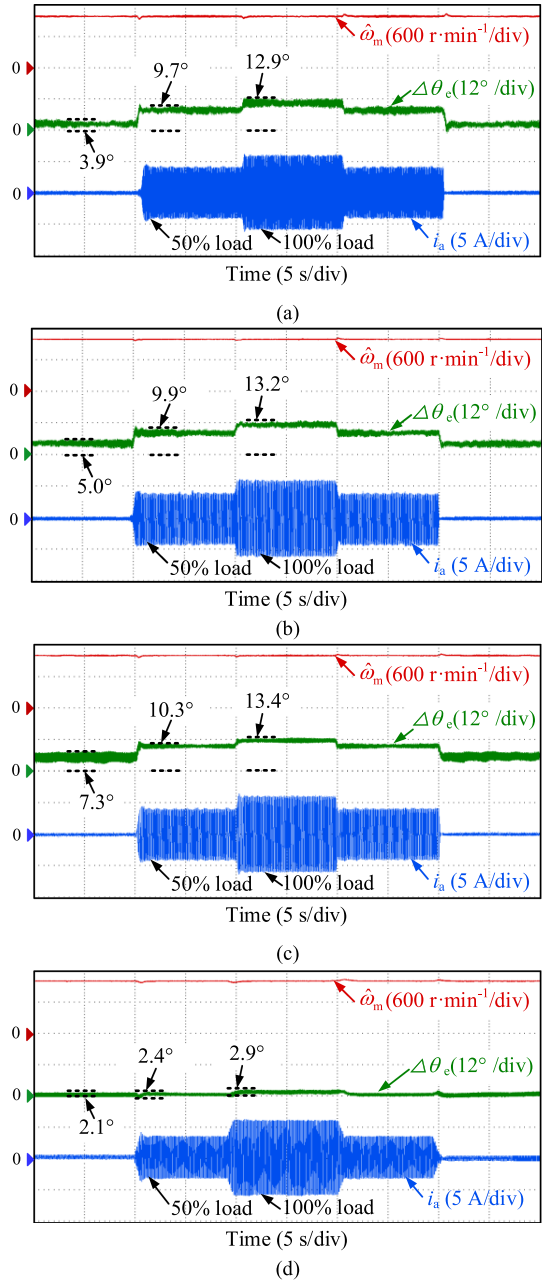

Fig. 20. Experimental results at 1000 r/min operation speed under 100% rated load, 50% rated load, and no-load conditions. (a) Second-order SOGI-based method. (b) TOGI-based method. (c) ROGI-based method. (d) Proposed SOGI-LCO-based method.

with load change condition. The coefficients, k_1 and k_2 of the second-order SOGI method are set as 1.56 and 3.11, respectively. The coefficients, k and k_0 of the TOGI method are set as 1.414 and 0.25, respectively. The coefficients k_r of the ROGI method is set as 1.414. It can be seen from Fig. 20(a), (b), (c), and (d) that the maximum rotor position estimation errors adopting the second-order SOGI-based method, the TOGI-based method, and the ROGI-based method are 12.9°, 13.2°, 13.4°, and 2.9°, respectively. The position estimation performance of the proposed method is better than that of the SOGI-based method.

Figs. 21 and 22 show 3-D Lissajous figure comparison of stator EMF and flux estimation results when the motor operates at 100 r/min with a sudden 100% rated load. It can be seen from Fig. 22 that the proposed method has an obvious convergence effect on limiting the stator EMF and flux trajectory loops, and the harmonic content in the trajectory is lower. In contrast, when using the SOGI method, the estimation results are more affected by the load in Fig. 21. The proposed SOGI-LCO algorithm has a better effect on suppressing the disturbance, which improves the robustness of the sensorless algorithm.

Figs. 23 and 24 show comparison results of the two algorithms, with 50% errors in resistance and inductance parameters, respectively. It can be seen from Fig. 23 that, with a 50% error in the resistance parameter, the position estimation error of the proposed method is 2.7°. The position estimation error of the SOGI method is 3.6° on the basis of the original 13.4° error. In Fig. 24, with a 50% error in the inductance parameter, the position estimation error of the proposed algorithm is 1.7°. The position estimation error of the SOGI method is 3.7° on the basis of the original 13.4° error. Therefore, the proposed method has a better parameter robustness than the SOGI method.

The experimental comparison results of position estimation error under different speeds (100–1000 r/min) and load conditions (0–100% of rated load) are shown in Fig. 25. In Fig. 25(a), the maximum position estimation error reaches 13.4° under 1000 r/min and 100% rated load. After adopting the proposed algorithm, the position estimation error is effectively suppressed, and the average error suppression rate exceeds over 60%.

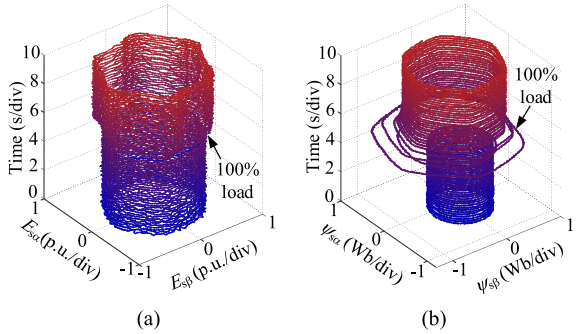

Fig. 21. 3-D Lissajous figure of estimate variables with the SOGI method. (a) $E_{s\alpha}$ and $E_{s\beta}$. (b) $\psi_{s\alpha}$ and $\psi_{s\beta}$.

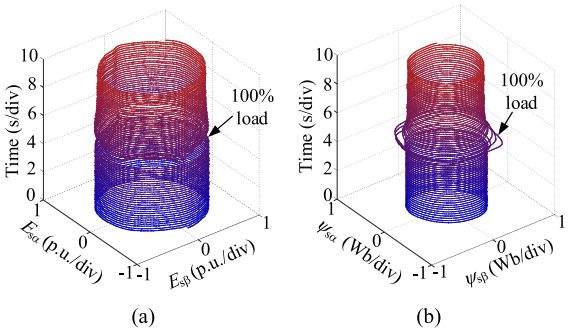

Fig. 22. 3-D Lissajous figure of estimate variables with the proposed method. (a) $E_{s\alpha}$ and $E_{s\beta}$. (b) $\psi_{s\alpha}$ and $\psi_{s\beta}$.

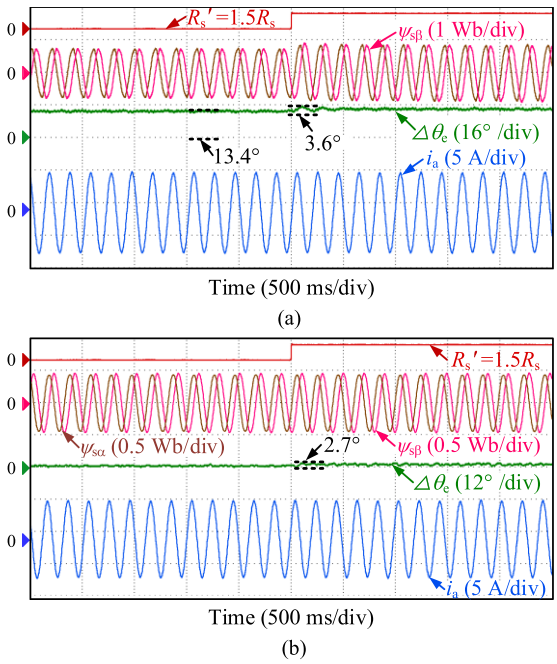

Fig. 23. Experimental results when resistance change 50%. (a) SOGI. (b) SOGI-LCO.

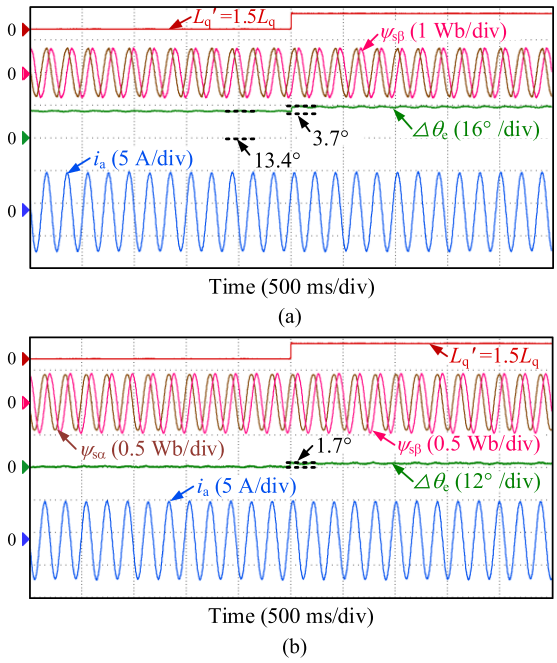

Fig. 24. Experimental results when inductance changes 50%. (a) SOGI. (b) SOGI-LCO.

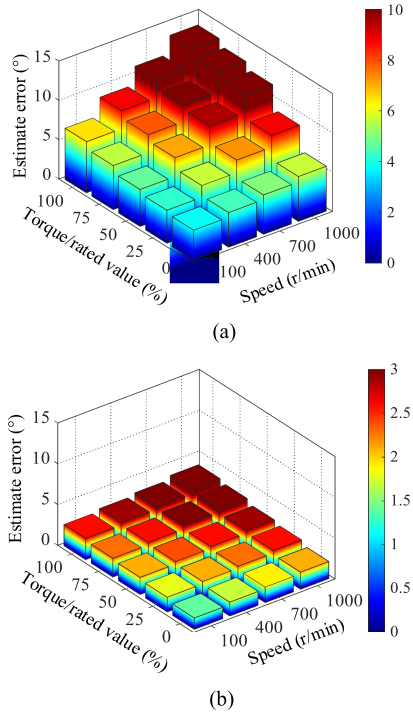

Fig. 25. Experimental comparison results of position estimation error under different speed and load conditions. (a) SOGI. (b) SOGI-LCO.

VI. Conclusion

An SOGI-LCO-based flux observer for sensorless PMSM drive has been proposed in this article, and its convergence and disturbance suppression effect are analyzed. With the advantage

of LCO, the estimated stator flux can converge to its set closed trajectory motion under external disturbances. Compared with the traditional position observation method based on SOGI, the proposed method has a better suppression ability for the position estimation error caused by parameter mismatch due to the self-excited oscillation function. The LCO structure can further optimize the suppression capability of the SOGI algorithm for harmonic components. Furthermore, the proposed method can enhance the harmonic suppress ability of SOGI, which improves the robustness of the model-based sensorless algorithms. Experimental results on the PMSM drive system verify the effectiveness of the proposed method.

REFERENCES

[1] J. Hang, H. Wu, S. Ding, Y. Huang, and W. Hua, "Improved loss minimization control for IPMSM using equivalent conversion method," *IEEE Trans. Power Electron.*, vol. 36, no. 2, pp. 1931–1940, Feb. 2021.

[2] G. Wang, M. Valla, and J. Solsona, "Position sensorless permanent magnet synchronous machine drives—A review," *IEEE Trans. Ind. Electron.*, vol. 67, no. 7, pp. 5830–5842, Jul. 2020.

[3] D. Xiao et al., "Universal full-speed sensorless control scheme for interior permanent magnet synchronous motors," *IEEE Trans. Power Electron.*, vol. 36, no. 4, pp. 4723–4737, Apr. 2021.

[4] L. Qian, L. Sun, K. Wang, and M. Tong, "Fusion of position estimation techniques for a swing servo by a permanent-magnet synchronous machine," *IEEE Trans. Ind. Electron.*, vol. 70, no. 7, pp. 6551–6562, Jul. 2023.

[5] G. Wang, R. Yang, and D. Xu, "DSP-based control of sensorless IPMSM drives for wide-speed-range operation," *IEEE Trans. Ind. Electron.*, vol. 60, no. 2, pp. 720–727, Feb. 2013.

[6] G. Zhang et al., "Hybrid pseudorandom signal injection for position sensorless SynRM drives with acoustic noise reduction," *IEEE Trans. Transport. Electrific.*, vol. 8, no. 1, pp. 1313–1325, Mar. 2022.

[7] Y. Wang, Y. Xu, and J. Zou, "ILC-based voltage compensation method for PMSM sensorless control considering inverter nonlinearity and sampling current DC bias," *IEEE Trans. Ind. Electron.*, vol. 67, no. 7, pp. 5980–5989, Jul. 2020.

[8] R. P. Burgos, P. Kshirsagar, A. Lidozzi, F. Wang, and D. Boroyevich, "Mathematical model and control design for sensorless vector control of permanent magnet synchronous machines," in *Proc. IEEE Workshops Comput. Power Electron.*, 2006, pp. 76–82.

[9] S. Medjmadj, D. Diallo, M. Mostefai, C. Delpha, and A. Arias, "PMSM drive position estimation: Contribution to the high-frequency injection voltage selection issue," *IEEE Trans. Energy Convers.*, vol. 30, no. 1, pp. 349–358, Mar. 2015.

[10] G. Zhang, G. Wang, D. Xu, and N. Zhao, "ADALINE-network-based PLL for position sensorless interior permanent magnet synchronous motor drives," *IEEE Trans. Power Electron.*, vol. 31, no. 2, pp. 1450–1460, Feb. 2016.

[11] B. Xu, L. Zhang, and W. Ji, "Improved non-singular fast terminal sliding mode control with disturbance observer for PMSM drives," *IEEE Trans. Transp. Electrific.*, vol. 7, no. 4, pp. 2753–2762, Dec. 2021.

[12] Z. Guchuan, A. Kaddouri, L. A. Dessaint, and O. Akhrif, "A nonlinear state observer for the sensorless control of a permanent-magnet AC machine," *IEEE Trans. Ind. Electron.*, vol. 48, no. 6, pp. 1098–1108, Dec. 2001.

[13] R. Dhaouadi, N. Mohan, and L. Norum, "Design and implementation of an extended Kalman filter for the state estimation of a permanent magnet synchronous motor," *IEEE Trans. Power Electron.*, vol. 6, no. 3, pp. 491–497, Jun. 1991.

[14] Z. Chen, M. Tomita, S. Doki, and S. Okuma, "An extended electromotive force model for sensorless control of interior permanent-magnet synchronous motors," *IEEE Trans. Ind. Electron.*, vol. 50, no. 2, pp. 288–295, Apr. 2003.

[15] G. Wang, T. Li, G. Zhang, X. Gui, and D. Xu, "Position estimation error reduction using recursive-least-square adaptive filter for model-based sensorless interior permanent-magnet synchronous motor drives," *IEEE Trans. Ind. Electron.*, vol. 61, no. 9, pp. 5115–5125, Sep. 2014.

[16] I. Boldea, M. C. Paicu, and G. D. Andreescu, "Active flux concept for motion-sensorless unified AC drives," *IEEE Trans. Power Electron.*, vol. 23, no. 5, pp. 2612–2618, Sep. 2008.

[17] T. C. Lin, Z. Q. Zhu, and J. M. Liu, "Improved rotor position estimation in sensorless-controlled permanent-magnet synchronous machines having asymmetric-EMF with harmonic compensation," *IEEE Trans. Ind. Electron.*, vol. 62, no. 10, pp. 6131–6139, Oct. 2015.

[18] N. R. N. Idris and A. H. M. Yatim, "An improved stator flux estimation in steady-state operation for direct torque control of induction machines," *IEEE Trans. Ind. Appl.*, vol. 38, no. 1, pp. 110–116, Jan. 2002.

[19] B. Yu et al., "A compensation strategy of flux linkage observer in SPMSM sensorless drives based on linear extended state observer," *IEEE Trans. Energy Convers.*, vol. 37, no. 2, pp. 824–831, Jun. 2022.

[20] Y. Park and S.-K. Sul, "Sensorless control method for PMSM based on frequency-adaptive disturbance observer," *IEEE Trans. Emerg. Sel. Topics Power Electron.*, vol. 2, no. 2, pp. 143–151, Jun. 2014.

[21] H. Wang, Y. Yang, X. Ge, Y. Zuo, Y. Yue, and S. Li, "PLL- and FLL-based speed estimation schemes for speed-sensorless control of induction motor drives: Review and new attempts," *IEEE Trans. Power Electron.*, vol. 37, no. 3, pp. 3334–3356, Mar. 2022.

[22] P. Rodríguez, A. Luna, I. Candela, R. Mujal, R. Teodorescu, and F. Blaabjerg, "Multiresonant frequency-locked loop for grid synchronization of power converters under distorted grid conditions," *IEEE Trans. Ind. Electron.*, vol. 58, no. 1, pp. 127–138, Jan. 2011.

[23] Y. Jiang, W. Xu, and C. Mu, "Improved SOIFO based nonlinear rotor flux observer for sensorless control of PMSM," in *Proc. IEEE Int. Annu. Conf. Ind. Electron. Soc.*, 2017, pp. 8219–8224.

[24] Y. Jiang, W. Xu, C. Mu, J. Zhu, and R. Dian, "An improved third-order generalized integral flux observer for sensorless drive of PMSMs," *IEEE Trans. Ind. Electron.*, vol. 66, no. 12, pp. 9149–9160, Dec. 2019.

[25] G. Wang et al., "Enhanced position observer using second-order generalized integrator for sensorless interior permanent magnet synchronous motor drives," *IEEE Trans. Energy Convers.*, vol. 29, no. 2, pp. 486–495, Jun. 2014.

[26] I. Boldea, M. C. Paicu, and G. D. Andreescu, "Active flux concept for motion-sensorless unified AC drives," *IEEE Trans. Power Electron.*, vol. 23, no. 5, pp. 2612–2618, Sep. 2008.

[27] S. Bolognani, S. Calligaro, and R. Petrella, "Design issues and estimation errors analysis of back-EMF-based position and speed observer for SPM synchronous motors," *IEEE Trans. Emerg. Sel. Topics Power Electron.*, vol. 2, no. 2, pp. 159–170, Jun. 2014.

[28] E. Oviedo, N. Vázquez, and R. Femat, "Synchronization technique of grid-connected power converters based on a limit cycle oscillator," *IEEE Trans. Ind. Electron.*, vol. 65, no. 1, pp. 709–717, Jan. 2018.

[29] M. Hinkkanen, T. Tuovinen, L. Harnefors, and J. Luomi, "A combined position and stator-resistance observer for salient PMSM drives: Design and stability analysis," *IEEE Trans. Power Electron.*, vol. 27, no. 2, pp. 601–609, Feb. 2012.

[30] J. Liu and Y. Zhang, "Performance improvement of nonlinear flux observer for sensorless control of PMSM," *IEEE Trans. Ind. Electron.*, vol. 70, no. 12, pp. 12014–12023, Dec. 2023.

[31] J. Yoo, H.-S. Kim, and S.-K. Sul, "Design of frequency-adaptive flux observer in PMSM drives robust to discretization error," *IEEE Trans. Ind. Electron.*, vol. 69, no. 4, pp. 3334–3344, Apr. 2022.

[32] W. Xu, Y. Jiang, C. Mu, and F. Blaabjerg, "Improved nonlinear flux observer-based second-order SOIFO for PMSM Sensorless Control," *IEEE Trans. Power Electron.*, vol. 34, no. 1, pp. 565–579, Jan. 2019.

[33] X. Yao, S. Huang, J. Wang, H. Ma, G. Zhang, and Y. Wang, "Improved ROGI-FLL-based sensorless model predictive current control with MRAS parameter identification for SPMSM drives," *IEEE Trans. Emerg. Sel. Topics Power Electron.*, vol. 11, no. 2, pp. 1684–1695, Apr. 2023.

Siqi Wang received the B.S. and M.S. degrees in electrical engineering from the Nanjing University of Aeronautics and Astronautics, Nanjing, China, in 2018 and 2021. He is currently working toward the Ph.D. degree in power electronics and electrical drives at the Harbin Institute of Technology, Harbin, China.

His current research interests include advanced control of permanent magnet synchronous motor drive and position sensorless control of ac motors.

Dawei Ding received the B.S. and M.S. degrees in electrical engineering from Hefei University of Technology, Hefei, China, in 2014 and 2017, respectively, and the Ph.D. degree in electrical engineering from Harbin Institute of Technology (HIT), Harbin, China, in 2021.

He is currently an Assistant Professor with School of Electrical Engineering and Automation, HIT. From 2020 to 2021, he was a visiting Ph.D. in Technical University of Denmark. He has authored more than 10 journal papers in IEEE Transactions and held nine authorized Chinese invention patents. His current research interests include advanced control of permanent magnet synchronous motor drives and electrolytic capacitorless ac motor drives.

Guoqiang Zhang (Senior Member, IEEE) received the B.S. degree in electrical engineering from Harbin Engineering University, Harbin, China, in 2011, and the M.S. and Ph.D. degrees in electrical engineering from Harbin Institute of Technology, Harbin, China, in 2013 and 2017, respectively.

Since 2017, he has been with the Department of Electrical Engineering, Harbin Institute of Technology, where he is currently an Associate Professor. His current research interests include control of electrical drives, and parameter identification technique, with main focus on sensorless field-oriented control of synchronous motor drives.

Dr. Zhang serves as an Associate Editor for *Journal of Power Electronics*.

Binxing Li received the B.S. degree in electrical engineering from the Harbin Institute of Technology, Weihai, China, in 2017. He is currently working toward the Ph.D. degree in power electronics and electrical drives at the Harbin Institute of Technology, Harbin, China.

His current research interests include permanent magnet synchronous motor drives, high efficiency ac–dc converter, and application of GaN power devices.

Qiwei Wang received the B.S., M.S., and Ph.D. degrees in electrical engineering, in 2015, 2017, and 2022, respectively, from the Harbin Institute of Technology, Harbin, China, where he is currently working toward the Postdoc in power electronics and electrical drives in the School of Electrical Engineering and Automation.

His current research interests include parameter identification technique, and PMSM position sensorless control.

Gaolin Wang (Senior Member, IEEE) received the B.S., M.S., and Ph.D. degrees in electrical engineering from Harbin Institute of Technology, Harbin, China, in 2002, 2004, and 2008, respectively.

In 2009, he joined the Department of Electrical Engineering, Harbin Institute of Technology as a Lecturer, where he has been a Full Professor of Electrical Engineering since 2014. From 2009 to 2012, he was a Postdoctoral Fellow with Shanghai Step Electric Corporation, where he was involved in the traction machine control for direct-drive elevators. He has authored more than 60 technical papers published in IEEE Transactions. He is the holder of 30 Chinese patents. His current major research interests include permanent magnet synchronous motor drives, position sensorless control of ac motors, and digital control of power converters.

Dr. Wang serves as a Guest Associate Editor of IEEE TRANSACTIONS ON INDUSTRIAL ELECTRONICS, an Associate Editor of IEEE TRANSACTIONS ON TRANSPORTATION ELECTRIFICATION, IET ELECTRIC POWER APPLICATIONS, and JOURNAL OF POWER ELECTRONICS.

Dianguo Xu (Fellow, IEEE) received the B.S. degree in control engineering from the Harbin Engineering University, Harbin, China, in 1982, and the M.S. and Ph.D. degrees in electrical engineering from the Harbin Institute of Technology (HIT), Harbin, China, in 1984 and 1989, respectively.

In 1984, he joined the Department of Electrical Engineering, HIT, as an Assistant Professor. Since 1994, he has been a Professor with the Department of Electrical Engineering, HIT. He was the Dean of the School of Electrical Engineering and Automation, HIT, from 2000 to 2010, and the Assistant President from 2010 to 2014. He is currently the Vice President of the HIT. He has authored or coauthored more than 600 technical papers. His research interests include renewable energy generation technology, power quality mitigation, sensorless vector-controlled motor drives, and high-performance PMSM servo system.

Dr. Xu is a Chairman of IEEE Harbin Section, Co-EIC of IEEE TRANSACTIONS ON POWER ELECTRONICS, Associate Editor of the IEEE TRANSACTIONS ON INDUSTRIAL ELECTRONICS, IEEE JOURNAL OF EMERGING AND SELECTED TOPICS IN POWER ELECTRONICS. He was the recipient of the 2018 IEEE IAS Outstanding Achievement Award.